Research Square

Preprints are preliminary reports that have not undergone peer review.
They should not be considered conclusive, used to inform clinical practice,
or referenced by the media as validated information.

Molecularly Tailored Halogen Bond Interactions Enabling Highly Reversible Four-Electron Iodine Conversion

Guanjie He

g.he@ucl.ac.uk

University College London https://orcid.org/0000-0002-7365-9645

Jingyu Wang

University College London

Yunpeng Zhong

University College London

Ling Chen

East China University of Science and Technology

Jiahao Zhang

East China University of Science and Technology

Wangxin Ge

East China University of Science and Technology

Ruwei Chen

University College London https://orcid.org/0009-0002-6429-6560

Hongliang Jiang

East China University of Science and Technology https://orcid.org/0000-0002-5243-3524

Zhiqian Guo

East China University of Science and Technology https://orcid.org/0000-0002-2192-825X

Hao Jiang

East China University of Science and Technology https://orcid.org/0000-0002-4388-6548

Chunzhong Li

East China University of Science and Technology https://orcid.org/0000-0001-7897-5850

Article

Keywords:

Posted Date: November 27th, 2026

DOI: https://doi.org/10.21203/rs.3.rs-11290280/v1

License: This work is licensed under a Creative Commons Attribution 4.0 International License.
Read Full License

Additional Declarations: There is **NO** Competing Interest.

Abstract

Aqueous four-electron zinc–iodine ($Zn–I_2$) batteries represent a promising route for sustainable grid-scale energy storage but remain fundamentally constrained by the long-standing interhalogen-stabilization paradigm, which relies on high-concentration, corrosive chloride electrolytes (up to 30 M) to stabilize hypervalent iodine species. This dependence poses sustainability and practical bottlenecks, necessitating fundamental breakthrough in stabilization strategy compatible with dilute, halogen-free electrolytes. Here, we establish a molecularly tailored halogen bond stabilization chemistry based on directional donor–acceptor interactions between nucleophilic amide molecules and electrophilic I^+ species. Within this framework, amide molecules act as halogen bond acceptors coordinatively deactivating the axial σ-holes of I^+ species to suppress irreversible hydrolysis while reconstructing the interfacial molecular environment. In situ spectroscopy, electrochemical investigations, and theoretical simulations establish a molecular-level relationship between halogen bond and hypervalent iodine reversibility, revealing that extended alkyl chains of halogen bond acceptor fortify the halogen bond interactions while mitigating interfacial H_2O, ensuring higher redox reversibility and interfacial stability. As a demonstration of this stabilization mechanism, four-electron $Zn–I_2$ cells achieve an energy density of 597.7 Wh kg^{-1} and stable operation in a 1.01 Ah pouch cell under dilute halogen-free electrolytes. This work provides a new stabilization paradigm to harness hypervalent iodine conversion through molecularly tailored halogen bond interactions, extending the scope of halogen bond chemistry toward electrochemical systems while providing new design principles for sustainable aqueous batteries.

Introduction

To tackle the hourly and seasonal fluctuations in renewable electricity output, aqueous zinc-based batteries have been at the forefront of sustainable grid-scale energy storage systems as their intrinsic safety, cost-effectiveness and natural abundance.[1–3] Among them, aqueous zinc–iodine ($Zn–I_2$) batteries are particularly attractive because four-electron conversion ($I^-/I^0/I^+$) simultaneously increases operating voltage and charge-storage capacity, delivering a theoretical energy density of 643.5 Wh kg^{-1}.[4–6] However, the practical implementation of this four-electron conversion reaction is hindered by the irreversible hydrolysis of hypervalent iodine species, which undermines the Coulombic efficiency and long-term cycling stability.[7,8] Existing attempts primarily relied on highly concentrated chloride electrolytes to supress I^+ hydrolysis through reduced water activity and ICl_2 interhalogens stabilization.[7,9,10] However, the inherent sustainability and economic advantage is compromised, while accelerating corrosion of standard battery components, severely limiting their broader applicability.[11–15] Although organic halides and halide-based ionic liquid additives have also been explored, they remain fundamentally dependent on the interhalogen-stabilization paradigm.[16–18] Consequently, establishing a sustainable stabilization paradigm that enables reversible hypervalent iodine conversion in dilute, halogen-free electrolytes has become a central challenge for practical aqueous $Zn–I_2$ batteries.

Achieving reversible four-electron iodine conversion fundamentally relies on rational regulation of interfacial microenvironment and stabilization chemistry of hypervalent iodine species, as systematically validated in our previous work.[19] Iodine conversion is intrinsically governed by interfacial reactions, where the interfacial microenvironment acts as a decisive gatekeeper that directs the iodine conversion pathway towards either reversible $I^-/I^0/I^+$ redox or irreversible hydrolysis. A through understanding of the intrinsic chemical nature of I^+ species is fundamental to establish effective stabilization chemistry. As a typical halonium ions, I^+ possesses highly electrophilic terminal σ-holes, endowing it with strong halogen bond donor capability.[20,21] According to the Pimentel–Rundle model, halonium ions tend to coordinate with two Lewis bases through directional three-center four-electron interactions, in which electron density from the Lewis bases is donated into the empty p-orbital lobes of I^+ to form halogen bond.[22] Such halogen bond chemistry have been extensively exploited in supramolecular structure and organic catalysis for stabilizing highly reactive intermediates.[23–25] Therefore, regulating the interfacial microenvironment through halogen bonding is theoretically promising for highly reversible four-electron iodine conversion. Correspondingly, a fundamental understanding of the intricate interplay among halogen bond chemistry, interfacial microenvironment, and electrochemical performances is therefore critical for establishing a new interfacial stabilization framework beyond the conventional interhalogen-stabilization paradigm, thereby paving the way for advanced reversible four-electron aqueous $Zn–I_2$ batteries.

Herein, we establish a molecularly tailored halogen bond stabilization chemistry using amides as representative halogen-bond acceptors. Resonance delocalization within the amide group enhances the Lewis basicity of the carbonyl oxygen, enabling directional coordination with electrophilic I^+ species (Fig. 1a).[26,27] Systematic variation of the alkyl chain lengths from acetamide (AA) to propionamide (PA) and butyramide (BA) effectively tuned the electronic and steric properties of these halogen bond acceptors, establishing a molecular-level relationship linking halogen bond interactions and electrochemical reversibility of hypervalent iodine (Fig. 1b).[28,29] Nuclear magnetic resonance (NMR) and *in situ* Raman spectroscopies, combined with molecular dynamics (MD) simulations, were performed to elucidate the interfacial stabilization mechanism, which involves restructuring the hydrogen bond network into halogen bond motif through the co-adsorption of kosmotropic anions and halogen bond acceptors on the electrified electrode surface. The modification effect positively correlates with the alkyl chain length of the amide molecules, as the hydrophobicity and Lewis basicity concurrently increase with chain elongation. Consequently, BA-coordinated $[I(BA)_2]^+$ motifs facilitated the strongest halogen bond interactions and established the most favorable H_2O-depleted interfacial microenvironment, allowing a remarkably enhanced redox reversibility and stability of iodine conversion (Fig. 1c). As a proof of concept, four-electron $Zn–I_2$ battery with BA as the halogen bond acceptor shows a high specific capacity (420.9 mAh g^{-1}) with high I^+ plateau contribution (150 mAh g^{-1}) and superior cycling stability (over 2,900 cycles at 5.0 A g^{-1}) in a chloride-free electrolyte at a very low concentration (3.4 mol L^{-1}). Techno-economic analysis further confirms the halogen bond stabilization chemistry offers improved sustainability and economic viability over the conventional interhalogen-stabilization paradigm, with a

levelized cost of storage of 256 USD MWh^{-1}. This work establishes a new paradigm for electrolyte engineering and molecular stabilization of hypervalent iodine conversion, pointing toward a promising direction for next-generation energy storage systems.

RESULTS AND DISCUSSION

Molecularly tailored halogen bond interactions. The chloride-free electrolyte consists of a $ZnSO_4$–$Zn(Ac)_2$–amide tri-component formulation, where amide molecules with different alkyl chain lengths (AA, PA, and BA) were investigated as halogen bond acceptors. The halogen bond stabilization chemistry was validated through first-principles calculations based on the density functional theory (DFT) method. Figure 2a displays the electrostatic potential (ESP) mappings of three types of amide molecules, providing a visualization of their charge spatial distribution. The results indicate that the carbonyl oxygen serves as a concentrated nucleophilic site, precisely anchoring the electrophilic σ-hole of I^+ through n→σ electronic transition, thereby establishing stable $[O\cdots I\cdots O]^+$ halogen bond motifs. The electron donating capability, *i.e.* Lewis basicity, increases with the extension of the alkyl chain (electron-donating group).[30,31] Among three amide molecules, BA exhibits the strongest electron-donating ability with an electrostatic potential of − 11.99 kcal mol^{-1} on the carbonyl oxygen, showing its higher capacity for halogen bonding compared to short-chain counterparts (− 10.61 kcal mol^{-1} in AA and − 11.76 kcal mol^{-1} in PA). As illustrated in **Figure S1**, all amide molecules exhibit lower binding energies towards I^+ than H_2O molecules, indicating their ability to impede hydrolysis through a higher affinity for hypervalent iodine species. Furthermore, the halogen bond strength correlates strongly with the halogen bond acceptor structure; the binding energy of $[I(BA)_2]^+$ is calculated to be 46.31 kJ mol^{-1}, which is much stronger than that of $[I(AA)_2]^+$ (30.87 kJ mol^{-1}) and $[I(PA)_2]^+$ (34.73 kJ mol^{-1}), following the same trend as Lewis basicity. To further unveil the impact of halogen bond chemistry on the cathodic interfacial environment, MD simulations were conducted under a bias potential of 1.8 V.[32,33] Detailed model and simulation parameters are described in Experimental section. After achieving equilibration (5000 ps), side- and top- snapshots of the cathodic interface were obtained (Fig. 2b and S2**)**. The analysis of the radial density distribution of interfacial species near the cathode (Fig. 2c and S3) reveals the enrichment of Ac^- anions and amide molecules at the Helmholtz plane. The kosmotropic Ac^- anions diminish the H_2O interaction with amide at the interface by destroying the hydrogen bond network.[34] Amide molecules, served as halogen bond acceptors, possess electrostatic interaction with iodine species, while their terminal alkyl chains repel water molecules.[26] Therefore, an interfacial microenvironment with reduced hydrogen bonding and enhanced halogen bonding is constructed.

The alkyl chain length of the halogen bond acceptors directly determines its hydrophobicity and Lewis basicity, resulting in different degrees of interfacial network reconstruction. A comparative analysis of different amide-modulated systems demonstrates that as the alkyl chain length increases, the density of amide molecules at the electrode interface rises, while the density of H_2O molecules decreases (Fig. 2d, e). The SAc-BA electrolyte achieves the highest amide density and the lowest H_2O density

simultaneously, forming a H_2O-depleted and halogen-bonding interfacial microenvironment at the cathode. Beyond the interfacial microenvironment, increasing the hydrophobic alkyl chain length further minimizes the number of solvated water molecules within the Zn^{2+} solvation shell and enhances compatibility at the Zn anode interface (**Figure S4-S6**). Collectively, by sequestering hypervalent iodine within robust $[I(BA)_2]^+$ motifs, this molecularly tailored halogen bond stabilization framework is theoretically promising for achieving highly reversible iodine conversion chemistry.

Reversible Iodine Conversion via Halogen Bond Stabilization. To explore the effect of halogen bond chemistry on the reversibility of iodine conversion reaction, cyclic voltammetry (CV) tests of Zn–I_2 full cells were performed in different amide-modified SAc electrolytes. As shown in **Figure S7**, in the SAc bare electrolyte, equilibrium for oxidation peak (O2, corresponding to the oxidation reaction from I^0 to I^+) is not reached at 1.9 V, and the corresponding reduction peak (R2) exhibits a negligible current response. This means the chemical irreversibility of I^0/I^+ conversion, which is caused by a chemical step following the electron transfer that transforms the product into another species, *i.e.* the representative EC coupled reaction.[35] Upon introducing halogen bond acceptors, two coupled redox peaks associated with a four-electron transfer reaction were observed in Fig. 3a. The conversion efficiency from I^+ to I^0 improves progressively with increasing alkyl chain length, as evidenced by the enhanced current response for R2 and the advance in the equilibrium potential for O2. The CV curve in the SAc-BA electrolyte exhibits the optimal reversible waves, indicating the stabilized $[I(BA)_2]^+$ halogen bond motifs effectively avert the subsequent hydrolysis of I^+. The peak potential separations for O1/R1 (ΔE_{p1}) in all three electrolytes are smaller than 57 mV, demonstrating the complete chemical and electrochemical reversibility of the I^-/I^0 conversion.[36] Whereas, O2/R2 bears a fairly slow electron transfer rate with relatively larger ΔE_{p2}.

To assess the improvement in I^0/I^+ reversibility across different halogen bond acceptors, peak current ratios ($i_{p,r}/i_{p,f}$) were conveniently calculated using the empirical method of Nicholson, as shown in Eq. 1[37]

$$\frac{i_{p,r}}{i_{p,f}} = \frac{i_{p,r0}}{i_{p,f}} + 0.48\frac{i_{\lambda}}{i_{p,f}} + 0.086$$

1

where $i_{p,r0}$ and $i_{p,f}$ are the peak currents in the reverse and forward potential scans, respectively, and i_λ is the current measured at the switching potential. For a fully reversible electron transfer reaction, $i_{p,r}$ should be equal to $i_{p,f}$. As illustrated in Fig. 3b, the peak current ratios increase steadily with the alkyl chain length and reach a quasi-reversible behavior with a ratio approximately to 1 in the SAc-BA electrolyte. Notably, the above analysis is performed at an ultra-low scan rate of 0.2 mV s^{-1}, ensuring that even at a sufficiently long timescale, the succeeding hydrolysis reaction is effectively isolated by the halogen bond chemistry mediated interfacial microenvironment. To further validate this trend, CV tests performed at scan rates (*v*) from 0.1 to 1 mV s^{-1} consistently exhibit two distinct redox couples for all

these systems (**Figure S8**). The linear dependence of i_p vs. $v^{1/2}$ for peak R2 and the corresponding coefficient of determination (R^2) are used to quantify the degree of electrochemically reversibility of I^0/I^+ redox (Fig. 3c**)**.[36,38] As the alkyl chain length increases, the R^2 values rise, reaching a maximumof 0.999 in the SAc-BA electrolyte, indicating the exceptionally chemical and electrochemical reversibility facilitated by $[O\cdots I\cdots O]^+$ halogen bond motifs. Additionally, Tafel slope analysis also reveals that BA coordination improves electron transfer kinetics of iodine conversion (Fig. 3d and S9).[39,40] To further understand the interfacial behavior and the role of halogen bond acceptors on charge transfer and mass transfer processes, *in-situ* electrochemical impedance spectroscopy (EIS) measurements were performed at different states of charge (SOC). As illustrated in Fig. 3e and S10, the Nyquist plots for all amide-modified SAc electrolytes exhibit a similar pattern, where the semicircle in the high-frequency region increases and subsequently decreases. Distribution of relaxation times (DRT) analysis was used to decouple the processes governing the EIS spectra during charging and discharging. The corresponding DRT plots show five peaks at timescales (τ) of 10^{-5},10^{-4},10^{-3} ~ 10^{-1}, 10^{-1}~10^{0} and 10^{1}, which are assigned to the Ohmic resistances, Zn-ion migration, charge transfer at the cathode, iodine-containing ions diffusion, and bulk ion-diffusion, respectively.[41,42] While $\tau1$, $\tau2$, and $\tau4$ maintain small and stable resistance values across different SOC states, the reaction kinetics are predominantly regulated by cathodic electron transfer ($\tau3$) and mass transfer ($\tau5$), particularly the latter (**Figure S11, S12**). A comparative analysis of R$\tau3$ and R$\tau5$ across different halogen bond acceptors indicates a progressive decline in these resistances with increasing alkyl chain length, indicating that the regulated interfacial microenvironment facilitates effective electron and mass transport throughout the charge-discharge cycle. (Fig. 3f, g). Correspondingly, a molecular-level relationship between halogen bond chemisry and the reversibility of iodine conversion reaction is established, where increasing alkyl chain length of halogen bond acceptors strengthens the halogen bond interactions and promotes a hydrophobic interfacial microenvironment, underpinning the chemical and electrochemical reversibility of iodine conversion.

Practical validation of the halogen bond stabilization chemistry. To evaluate the efficacy of proposed halogen bond stabilization strategy, four-electron Zn–I_2 batteries were adopted for experimental verification. The galvanostatic charge/discharge voltage profile in the SAc bare electrolyte shows no high-voltage discharge plateau at a current density of 1 A g^{-1}, suggesting that the chemically irreversible nature of hypervalent iodine species (**Figure S13**). Upon the introduction of the halogen bond acceptors, a well-defined four-electron iodine conversion process emerges, as evidenced by two characteristic discharge plateaus at ~ 1.7 V (I^+ to I^0) and ~ 1.2 V (I^0 to I^-), respectively (Fig. 4a**)**, aligning with the observations presented in Fig. 3a. Notably, the capacity contribution of the high-voltage redox couple is maximized in the SAc-BA electrolyte (~ 150 mAh g^{-1}), significantly outperforming the short-chain counterparts (~ 60 mAh g^{-1} in SAc-AA and ~ 100 mAh g^{-1} in SAc-PA). This enhanced capacity leads to a higher overall specific capacity of 420.9 mAh g^{-1} (~ 328.5 mAh g^{-1} in SAc-AA and ~ 380.3 mAh g^{-1} in SAc-PA) and an increased average discharge voltage of 1.42 V (1.30 V in SAc-AA and 1.35 V in SAc-PA) at a current density of 1 A g^{-1}. It should be mentioned that a specific capacity of 26.4 mA h g^{-1}

(equivalent to ~67.9 mA h g^{-1} based on iodine mass) originates from the supplementary contribution of the activated carbon (AC) host (**Figure S13)**.

As depicted in Fig. 4b, Zn–I_2 cells employing the SAc-BA electrolyte exhibit significantly superior rate capability and CE compared to those with SAc-AA or SAc-PA electrolytes, demonstrating enhanced kinetics and reversibility. Figure 4c **and Table S1** futher highlight the exceptional energy density of four-electron conversion Zn–I_2 cells based on the SAc-BA electrolyte (597.7 Wh kg^{-1}), substantially surpassing its short-chain counterparts (427.1 Wh kg^{-1} in SAc-AA and 513.4 Wh kg^{-1} in SAc-PA), as well as other reported zinc-based batteries. Consequently, the Zn–I_2 cell with the SAc-BA electrolyte can operate over 2,900 cycles, even at a large current density of 5 A g^{-1}, with a low-capacity decay of only 0.007% per cycle (Fig. 4d). These results confirm that the halogen bond interactions mediated H_2O-depleted and halogen-bonding interfacial structure can effectively inhibit the hydrolysis of hypervalent iodine species, playing a vital role in enhancing the performance of four-electron conversion Zn–I_2 batteries. Moreover, the hydrophobic alkyl chain length of the halogen bond acceptors is of great importance for the stability improvement. More importantly, the designed SAc-BA electrolyte system achieves highly reversible $I^-/I^0/I^+$ redox reactions at extremely low-cost, low-concentration and chloride-free conditions, offering substantial benefits over other reported electrolytes of aqueous Zn–I_2 batteries (Fig. 4e **and Table S2**). To evaluate its practical implementations, Zn–I_2 pouch cell based on SAc-BA electrolyte was assembled using double-sided coated electrodes with a high iodine loading of 11.0 mg cm^{-2} and a footprint of 10×10 cm^2 (Fig. 4f). This cell exhibits a high capacity of 1.01 Ah and maintains a remarkable capacity retention of 99.2% and an average coulombic efficiency (CE) of 99.1% over 764 cycles, providing compelling validation for the practical viability of the halogen bond stabilization chemistry (Fig. 4g).

Halogen bond stabilization mechanism. As illustrated in Fig. 5a, amide molecules engage in hydrogen bonding with water molecules, where the carbonyl oxygen behaves as a hydrogen bond acceptor and the amino group acts as a hydrogen bond donor.[43] Upon introduction into the SAc bare electrolyte, sulfate and acetate anions served as kosmotropic anions that can disrupt the hydrogen bond network of amide molecules, rendering them more hydrophobic.[44] Consequently, in the four-electron Zn–I_2 configuration, amide molecules enrich at the electrode surface and engage in directional donor–acceptor interactions to construct robust $[I(BA)_2]^+$ halogen bond motifs, thereby stabilizing the highly reactive hypervalent iodine species. The reduction in hydrogen bonding is attested by the NMR spectroscopy. In the BA-D_2O system, the protons within the amino group resonate at a relatively high frequency, suggesting a lower electron cloud density due to the electron deshielding effect of hydrogen bonding (Fig. 5b). Futhermore, the upfield shfit of the ^1H NMR signal in the SAc-BA system confirms that kosmotropic anions weaken the interactions between BA and D_2O. To quantify this attenuation, the chemical shift variations for each proton within the amide molecule were compared (Fig. 5c). Compared to short-chain amides, BA exhibits the highest change values, suggesting a notable weakening of the hydrogen bond network surrounding the entire BA molecule in the SAc electrolyte. The formation of halogen bond is further confirmed by *in*

situ Raman spectroscopy. The I···O symmetric stretching vibrations in the $[I(BA)_2]^+$ halogen bond motifs appear at around 249 cm^{-1}, which intensifies during the charging process and subsequently diminishes and disappears upon the discharge process (Fig. 5d).[9,45,46] To capture real-time halogen-bonding dynamics, a series of *in-situ* Raman mappings were conducted over a 38 μm × 28 μm region (Fig. 5e**)**. The SAc-BA electrolyte demonstrates a significantly higher density of halogen bonding at the electrode surface, with stronger retention at the beginning of the discharge process due to its enhanced halogen bond strength. By unveiling the dynamic transition from hydrogen bond dissociation to halogen bond formation, these findings establish molecularly tailored halogen bonding as a new stabilization mechanism that transcends the conventional interhalogen-stabilization paradigm to enable highly reversible four-electron iodine conversion.

Techno-economic validation of the halogen bond stabilization chemistry. Beyond electrochemical performance, the practical deployment of four-electron Zn–I_2 batteries ultimately depends on their techno-economic viability. To validate the sustainability and commercial potential of the proposed halogen bond stabilization mechanism, a cell-level techno-economic assessment was performed using the Battery Performance and Cost (BatPaC) model.[47] Compared with conventional chloride-concentrated systems, the dilute halogen-free electrolyte eliminates excessive salt consumption and corrosion-resistant current collectors, reducing the total cell cost from 399.0 USD kWh^{-1} to 79.7 USD kWh^{-1}, corresponding to an approximately fivefold reduction (Fig. 6a). In addition to cell-level cost, the practical viability of energy storage systems hinges on the levelized cost of storage (LCOS), which normalizes lifespan cost per unit of cumulative delivered electricity.[48] System-level assessment further demonstrates an LCOS of 256 USD MWh^{-1} under a representative 1 MW/2 MWh energy-storage scenario, outperforming representative aqueous battery technologies while approaching the U.S. Department of Energy target (Fig. 6b **and Table S3-8**).[49–52] Cost breakdown and sensitivity analysis identify cell replacement and electricity consumption as the dominant cost drivers and indicate that further improvements in round-trip efficiency and cycling durability could reduce the LCOS to 230 and 162 USD MWh^{-1}, respectively (Fig. 6c-d). Collectively, these results provide techno-economic validation of the proposed halogen bond stabilization mechanism. By replacing the conventional interhalogen-stabilization paradigm, this electrolyte design simultaneously enables reversible four-electron iodine conversion, lowers cell cost, and improves projected system economics under practical dilute, halogen-free conditions (Fig. 6e **and Table S9**).

Conclusion

In conclusion, we highlight the molecularly tailored halogen bond interactions that achieve highly reversible hypervalent iodine conversion beyond the conventional interhalogen-stabilization paradigm in high-concentration and corrosive chloride-containing electrolytes. By integrating molecular design, in situ spectroscopy, and multiscale simulations, we reveal how cooperative halogen bond interactions reconstruct the interfacial microenvironment to stabilize hypervalent iodine species while suppressing hydrolysis. Furthermore, we establish, for the first time, a molecular-level relationship linking halogen

bond acceptor structure, halogen bond strength, interfacial microenvironment, and the reversibility of hypervalent iodine conversion. This molecular stabilization enables highly reversible four-electron Zn–I_2 batteries with long-term cycling stability exceeding 2,900 cycles in a dilute, halogen-free electrolyte while improving the projected techno-economic competitiveness of the system. This work establishes a novel stabilization strategy for hypervalent iodine conversion through molecularly tailored halogen-bond chemistry, providing a generalized electrolyte engineering framework for practical rechargeable halogen-based conversion systems.

Declarations

Data availability

Data supporting findings of this work are available within this article and its Supplementary Information. Source data are provided with this paper.

Acknowledgments

The authors acknowledge the Engineering and Physical Sciences Research Council (EPSRC, EP/V027433/3), the UK Research and Innovation (UKRI) under the UK Government's Horizon Europe funding guarantee (101077226; EP/ Y008707/1 and EP/Z003083/1), the National Natural Science Foundation of China (22608174) and the Shanghai Pujiang Program (25PJD5029). J.W. acknowledges the support from Chinese Scholarship Council and the BatPaC for techno-economic analysis.

Author Contributions

J. Y. W. and Y. P. Z. contributed equally. J. Y. W., R. W. C., and G.J.H. conceived this work. J. Y. W. designed and conducted the experiments. J. Y. W. wrote the manuscript. R. W. C., J. H, and G.J.H. supervised the research and edited the manuscript. All authors contributed to measurements and data analysis.

Competing interests

The authors declare no competing interest.

References

1. Tang, L.; Peng, H.; Kang, J.; Chen, H.; Zhang, M.; Liu, Y.; Kim, D. H.; Liu, Y.; Lin, Z. Zn-Based Batteries for Sustainable Energy Storage: Strategies and Mechanisms. *Chem. Soc. Rev.* **2024**, *53* (10), 4877–4925.
2. Liang, Y.; Yao, Y. Designing Modern Aqueous Batteries. *Nat. Rev. Mater.* **2022**, *8* (2), 109–122.
3. Dong, Y.; Hu, H.; Liang, P.; Xue, L.; Chai, X.; Liu, F.; Yu, M.; Cheng, F. Dissolution, Solvation and Diffusion in Low-Temperature Zinc Electrolyte Design. *Nat. Rev. Chem.* **2025**, *9*, 102–117.

4. Li, X.; Xu, W.; Zhi, C. Halogen-Powered Static Conversion Chemistry. *Nat. Rev. Chem.* **2024**, *8*, 359–375.
5. Kundu, D.; Adams, B. D.; Duffort, V.; Vajargah, S. H.; Nazar, L. F. A High-Capacity and Long-Life Aqueous Rechargeable Zinc Battery Using a Metal Oxide Intercalation Cathode. *Nat. Energy* **2016**, *1*, 16119.
6. Zou, Y.; Liu, T.; Du, Q.; Li, Y.; Yi, H.; Zhou, X.; Li, Z.; Gao, L.; Zhang, L.; Liang, X. A Four-Electron Zn-I_2 Aqueous Battery Enabled by Reversible $I^-/I_2/I^+$ Conversion. *Nat. Commun.* **2021**, *12*, 170.
7. Zong, W.; Li, J.; Zhang, C.; Dai, Y.; Ouyang, Y.; Zhang, L.; Li, J.; Zhang, W.; Chen, R.; Dong, H.; Gao, X.; Zhu, J.; Parkin, I. P.; Shearing, P. R.; Lai, F.; Amine, K.; Liu, T.; He, G. Dynamical Janus Interface Design for Reversible and Fast-Charging Zinc–Iodine Battery under Extreme Operating Conditions. *J. Am. Chem. Soc.* **2024**, *146* (31), 21377–21388.
8. Palmer, D. A.; Ramette, R. W.; Mesmer, R. E.; The Hydrolysis of Iodine: Equilibria at High Temperatures. *J. Nucl. Mater.* **1985**, *130*, 280–286.
9. Li, W.; Xu, H.; Zhang, H.; Wei, F.; Zhang, T.; Wu, Y.; Huang, L.; Fu, J.; Jing, C.; Cheng, J.; Liu, S. Designing Ternary Hydrated Eutectic Electrolyte Capable of Four-Electron Conversion for Advanced Zn–I_2 Full Batteries. *Energy Environ. Sci.* **2023**, *16* (10), 4502–4510.
10. Liang, G.; Liang, B.; Chen, A.; Zhu, J.; Li, Q.; Huang, Z.; Li, X.; Wang, Y.; Wang, X.; Xiong, B.; Jin, X.; Bai, S.; Fan, J.; Zhi, C. Development of Rechargeable High-Energy Hybrid Zinc-Iodine Aqueous Batteries Exploiting Reversible Chlorine-Based Redox Reaction. *Nat. Commun.* **2023**, *14*, 1856.
11. Liu, T.; Lei, C.; Wang, H.; Xu, C.; Ma, W.; He, X.; Liang, X. Practical Four-Electron Zinc-Iodine Aqueous Batteries Enabled by Orbital Hybridization Induced Adsorption-Catalysis. *Sci. Bull.* **2024**, *69* (11), 1674–1685.
12. Liu, T.; Lei, C.; Wang, H.; Li, J.; Jiang, P.; He, X.; Liang, X. Aqueous Electrolyte with Weak Hydrogen Bonds for Four-Electron Zinc-Iodine Battery Operates in a Wide Temperature Range. *Adv. Mater.* **2024**, *36* (32), e2405473.
13. Liu, T.; Lei, C.; Wang, H.; Yang, W.; He, X.; Liang, X. Triflate Anion Chemistry for Enhanced Four-Electron Zinc–Iodine Aqueous Batteries. *Chem. Commun.* **2024**, *60*, 7447–7450.
14. Efaw, C. M.; Wu, Q.; Gao, N.; Zhang, Y.; Zhu, H.; Gering, K.; Hurley, M. F.; Xiong, H.; Hu, E.; Cao, X.; Xu, W.; Zhang, J.-G.; Dufek, E. J.; Xiao, J.; Yang, X.-Q.; Liu, J.; Qi, Y.; Li, B. Localized High-Concentration Electrolytes Get More Localized through Micelle-Like Structures. *Nat. Mater.* **2023**, *22* (12), 1531–1539.
15. Tutusaus, O.; Mohtadi, R.; Arthur, T. S.; Mizuno, F.; Nelson, E. G.; Sevryugina, Y. V. An Efficient Halogen-Free Electrolyte for Use in Rechargeable Magnesium Batteries. *Angew. Chem. Int. Ed. Engl.* **2015**, *54* (27), 7900–7904.
16. Hu, Z.; Han, Z.; Liu, H.; Jiang, X.; Bai, K.; Huang, S.; Yang, Z.; Ye, M.; Tang, Y.; Zhang, Y.; Liu, X.; Wen, Z.; Park, H.; Li, C. Mechanically Strong and Tough Ionic Liquid Gel Electrolyte for Four Electron Zinc–Iodine Batteries. *J. Am. Chem. Soc.* **2025**, *147* (50), 46632–46641.

17. Huang, H.; Shi, Z.; Chen, L.; Qi, J.; Feng, Z.; Liu, G.; Ye, M.; Zhang, Y.; Wen, Z.; Liu, X.; Wei, Y.; Tang, Y.; Li, C. Organo-Interhalogen Chemistry Enables High-Voltage Bromine Redox for Stable Zinc Batteries. *Energy Environ. Sci.* **2026**, *19* (5), 1658–1668.
18. Shi, Z.; Tang, Y.; Wei, Y.; Liu, G.; Huang, H.; Qi, J.; Feng, Z.; Ye, M.; Zhang, Y.; Wen, Z.; Liu, X.; Yang, Q.; Zhi, C.; Li, C. Carbon-Halogen Bond Substitution Enables High-Utilization Four-Electron Iodine Redox in Noncorrosive Dilute Electrolytes. *Nat. Commun.* **2026**, *17*, 3048.
19. Chen, R.; Dong, H.; Dai, Y.; Wang, J.; Chen, J.; Liu, J.; Feng, J.; Zhong, Y.; Zong, W.; Zhang, W.; Yang, H.; Cui, Z.; He, G. Low-Concentration and Non-Halogen Aqueous Electrolytes to Achieve Reversible Four-Electron Iodine Conversion Reactions. https://doi.org/10.21203/rs.3.rs-6372434/v1
20. Cavallo, G.; Metrangolo, P.; Milani, R.; Pilati, T.; Priimagi, A.; Resnati, G.; Terraneo, G. The Halogen Bond. *Chem. Rev.* **2016**, *116* (4), 2478–2601.
21. Kellett, C. W.; Kennepohl, P.; Berlinguette, C. P. π Covalency in the Halogen Bond. *Nat. Commun.* **2020**, *11*, 3310.
22. Turunen, L.; Erdelyi, M. Halogen Bonds of Halonium Ions. *Chem. Soc. Rev.* **2020**, *49* (9), 2688–2700.
23. Turunen, L.; Warzok, U.; Schalley, C. A.; Rissanen, K. Nano-Sized $I_{12}L_6$ Molecular Capsules Based on the [N···I^+···N] Halogen Bond. *Chem* **2017**, *3* (5), 861–869.
24. Bai, X.; Tian, Z.; Dong, H.; Xia, N.; Zhao, J.; Sun, P.; Gong, G.; Wang, J.; Wang, L.; Li, H.; Chen, S. Halogen-Bonded Organic Frameworks (XOFs) Based on N···Br^+···N Bonds: Robust Organic Networks Constructed by Fragile Bonds. *Angew. Chem. Int. Ed.* **2024**, *63* (35), e202408428.
25. Warzok, Ulrike.; Marianski, M.; Hoffmann, W.; Turunen, L.; Rissanen, K.; Pagel, K.; Schalley, C. A. Surprising Solvent-Induced Structural Rearrangements in Large [N···I^+···N] Halogen-Bonded Supramolecular Capsules: An Ion Mobility-Mass Spectrometry Study. *Chem. Sci.* **2018**, *9* (44), 8343–8351.
26. Kemnitz, C. R.; Loewen, M. J. "Amide Resonance" Correlates with a Breadth of C–N Rotation Barriers. *J. Am. Chem. Soc.* **2007**, *129* (9), 2521–2528.
27. Szostak, R.; Szostak, M. Chemistry of Bridged Lactams: Recent Developments. *Molecules* **2019**, *24* (2), 274.
28. Velasquez, J. D.; Echevrría, J.; Alvarez, S. Structure and Bonding of Halonium Compounds. *Inorg. Chem.* **2023**, *62* (23), 8980–8992.
29. Vallejo Narvaez, W. E.; Jimenez, E. I.; Romero-Montalvo, E.; Sauza-de la Vega, A.; Quiroz-Garcia, B.; Hernandez-Rodriguez, M.; Rocha-Rinza, T. Acidity and Basicity Interplay in Amide and Imide Self-Association. *Chem. Sci.* **2018**, *9* (19), 4402–4413.
30. Oliveri, I. P.; Maccarrone, G.; Di Bella, S. A Lewis Basicity Scale in Dichloromethane for Amines and Common Nonprotogenic Solvents Using a Zinc(II) Schiff-Base Complex as Reference Lewis Acid. *J. Org. Chem.* **2011**, *76* (21), 8879–8884.
31. Laurence, C.; Graton, J.; Gal, J.-F. An Overview of Lewis Basicity and Affinity Scales. *J. Chem. Educ.* **2011**, *88* (12), 1651–1657.

32. Thompson, A. P.; Aktulga, H. M.; Berger, R.; Bolintineanu, D. S.; Brown, W. M.; Crozier, P. S.; in 't Veld, P. J.; Kohlmeyer, A.; Moore, S. G.; Nguyen, T. D.; Shan, R.; Stevens, M. J.; Tranchida, J.; Trott, C.; Plimpton, S. J.; LAMMPS - A Flexible Simulation Tool for Particle-Based Materials Modeling at the Atomic, Meso, and Continuum Scales. *Comput. Phys. Commun.* **2022**, 271, 108171.
33. Ge, W.; Chen, Y.; Fan, Y.; Zhu, Y.; Liu, H.; Song, L.; Liu, Z.; Lian, C.; Jiang, H.; Li, C. Dynamically Formed Surfactant Assembly at the Electrified Electrode-Electrolyte Interface Boosting CO_2 Electroreduction. *J. Am. Chem. Soc.* **2022**, *144* (14), 6613–6622.
34. Gregory, K. P.; Elliott, G. R.; Robertson, H.; Kumar, A.; Wanless, E. J.; Webber, G. B.; Craig, V. S. J.; Andersson, G. G.; Page, A. J. Understanding Specific Ion Effects and the Hofmeister Series. *Phys. Chem. Chem. Phys.* **2022**, *24* (21), 12682–12718.
35. Sandford, C.; Edwards, M. A.; Klunder, K. J.; Hickey, D. P.; Li, M.; Barman, K.; Sigman, M. S.; White, H. S.; Minteer, S. D. A Synthetic Chemist's Guide to Electroanalytical Tools for Studying Reaction Mechanisms. *Chem. Sci.* **2019**, *10* (26), 6404–6422.
36. Elgrishi, N.; Rountree, K. J.; McCarthy, B. D.; Rountree, E. S.; Eisenhart, T. T.; Dempsey, J. L. A Practical Beginner's Guide to Cyclic Voltammetry. *J. Chem. Educ.* **2017**, *95* (2), 197–206.
37. Nicholson, R. S. Semiempirical Procedure for Measuring with Stationary Electrode Polarography Rates of Chemical Reactions Involving the Product of Electron Transfer. *Anal. Chem.* **1966**, *38* (10), 1406.
38. Osteryoung, J. Voltammetry for the future. *Acc. Chem. Res.* **1993**, *26* (3), 77–83.
39. Hu, T.; Zhao, Y.; Yang, Y.; Lv, H.; Zhong, R.; Ding, F.; Mo, F.; Hu, H.; Zhi, C.; Liang, G. Development of Inverse-Opal-Structured Charge-Deficient Co_9S_8@Nitrogen-Doped-Carbon to Catalytically Enable High Energy and High Power for the Two-Electron Transfer I^+/I^- Electrode. *Adv. Mater.* **2024**, *36* (18), 2312246.
40. Li, M.; Huang, Z.; Liang, Y.; Wu, Z.; Zhang, H.; Chen, H.; Zhang, S. Accelerating Lithium-Ion Transfer and Sulfur Conversion via Electrolyte Engineering for Ultra-Stable All-Solid-State Lithium–Sulfur Batteries. *Adv. Funct. Mater.* **2024**, *35* (3), 2413580.
41. Chen, J.; Quattrocchi, E.; Ciucci, F.; Chen, Y. Charging Processes in Lithium-Oxygen Batteries Unraveled through the Lens of the Distribution of Relaxation Times. *Chem* **2023**, *9* (8), 2267–2281.
42. Soni, R.; Robinson, J. B.; Shearing, P. R.; Brett, D. J. L.; Rettie, A. J. E.; Miller, T. S. Lithium-Sulfur Battery Diagnostics through Distribution of Relaxation Times Analysis. *Energy Storage Mater.* **2022**, *51*, 97–107.
43. Zhou, L.; Tian, S.; Du, X.; Liu, T.; Zhang, H.; Zhang, J.; Hu, S.; Chen, Z.; Zhang, J.; Cui, G. Suppressing Hydrogen Evolution in Aqueous Lithium-Ion Batteries with Double-Site Hydrogen Bonding. *ACS Energy Lett.* **2023**, *8* (1), 1, 40–47.
44. Cao, G.; Zhao, L.; Ji, X.; Peng, Y.; Yu, M.; Wang, X.; Li, X.; Ran, F. "Salting out" in Hofmeister Effect Enhancing Mechanical and Electrochemical Performance of Amide-Based Hydrogel Electrolytes for Flexible Zinc-Ion Battery. *Small* **2023**, *19* (30), e2207610.

45. Klaboe, P. The Raman Spectra of Some Iodine, Bromine, and Iodine Monochloride Charge-Transfer Complexes in Solution. *J. Am. Chem. Soc.* **1967**, *89* (15), 3667–3676.
46. Maes, G. The Infrared and Raman Intensity of the Halogen Stretching Vibrations in Complexes of Iodine and Bromine with Pyridines. *J. Mol. Struct.* **1980**, *61*, 95–100.
47. Knehr, K.; Kubal, J.; Nelson, P.; Ahmed, S. Battery Performance and Cost Modeling for Electric-Drive Vehicles (a manual for BatPaC v5.0). Argonne National Lab. (ANL), Argonne, IL United States, **2022**.
48. Oliver, S.; Sylvain, M.; Adam, H.; Iain, S. Projecting the Future Levelized Cost of Electricity Storage Technologies. *Joule* **2019**, *3*, 81–100.
49. Wei, Z.; Wang, Y.; Hong, H.; Chen, Z.; Cheng, A.; Wang, S.; Yang, S.; Hou, Y.; Huang, Z.; Liang, G.; Zhi, C. Long-Life Aqueous Zinc-Iodine Flow Batteries Enabled by Selectively Intercepting Hydrated Ions. *Nat. Commun.* **2025**, *16*, 9301.
50. Diana, C.; Giuseppina, D.; Guido, F.; Aldo, B.; Andrea, B.; Lorenzo, F. Techno-economic analysis of Aqueous Organic Redox Flow Batteries: Stochastic Investigation of Capital Cost and Levelized Cost of Storage. *Appl. Energy* **2024**, *360*, 122738.
51. Behnam, Z.; Sanna S. Electrical Energy Storage Systems: A Comparative Life Cycle Cost Analysis. *Renew. Sustain. Energy Rev.* **2015**, *42*, 569–596.
52. U.S. Department of Energy. Achieving the Promise of Low-Cost Long Duration Energy Storage. U.S. Department of Energy, **2024**, https://www.energy.gov/oe/storage-innovations-2030.

Methods

Electrode preparation

The I_2@activated carbon (I_2@AC) cathode was prepared by gas-adsorption method. Iodine (Sigma-Aldrich) and activated carbon powder (Kuraray, YP-80F) were homogeneously mixed with a mass ratio of 1:1 and heated at 120 °C for 6 h under sealed conditions. The mass loading of iodine was determined to be 28 wt% by thermogravimetry. The cathode materials, Super-P (Sigma-Aldrich) and polyvinylidene fluoride (Sigma-Aldrich) were mixed in the N-methyl-2-pyrrolidone with a mass ratio of 7:2:1. The slurry was uniformly coated on the carbon paper (Toray, TGP-H060) and dried for 3 h. The mass loading of the I_2@AC was about 5 mg cm^{-2}.

Electrolyte preparation

The chloride-free electrolytes for four-electron zinc-iodine battery were prepared by using $ZnSO_4 \cdot 7H_2O$ (Sigma-Aldrich) and $Zn(CH_3COO)_2 \cdot 2H_2O$ (Sigma-Aldrich) as zinc salts and a series of amides (Sigma-Aldrich) as additives. For the baseline electrolyte, 2.4 M $ZnSO_4$ and 0.6 M $Zn(Ac)_2$ were mixed in deionized water, denoted as the SAc electrolyte. 0.4 M of acetamide (AA), propionamide (PA) and butyramide (BA) were dissolved into the SAc electrolyte and ultrasonically treated for 30 min to obtain SAc-AA, SAc-PA and SAc-BA electrolytes, respectively.

Material characterization

Thermogravimetric analysis (TGA, NETZSCH TG209F1 Libra) was carried out to determine the mass loading of iodine in I_2@AC. The ^{1}H nuclear magnetic resonance (NMR) spectra were recorded on Bruker Avance III 500 NMR spectrometer. *In-situ* Raman spectra and mappings (with area of 38 μm × 28 μm) were recorded on Bruker SENTERRA II confocal Raman microscope with a 532 nm laser. The morphologies of cycled Zn anodes were imaged by scanning electron microscope (SEM, JEOL-7600, 15 kV).

Electrochemical measurements

The electrochemical performances for Zn–I_2 full cells, Zn||Zn symmetric cells, Zn||Cu and Zn||Ti asymmetric cells were assembled using 316 stainless steel CR2025 coin cells in the open-air environment. Zn foils with 100 μm thickness were utilized as anodes. Glass-fiber (Whatman, GF/D) was adopted as the separator. The electrolyte usage for each coin cell was 100 μL. The cyclic voltammetry (CV) and linear sweep voltammetry (LSV) profiles were collected using the Biologic VMP3 potentiostat. The galvanostatic charge-discharge (GCD) was tested by Neware battery testing system with a voltage range of 0.6-1.8 V. Corrosion tests were conducted in a standard three-electrode system, where the Pt wire, saturated Ag/AgCl electrode, 316 stainless steels were used as the counter, reference and working electrodes, respectively. For pouch cell assembly, two large-area I_2@AC cathodes (10 × 10 cm^2) were pressed onto both sides of a pretreated Ti mesh current collector. Zn foils (11 × 11 cm^2) and Olegeeino GF/D glass-fiber (12 × 12 cm^2) served as anodes and separators, respectively. Ti foils were attached to the electrodes as tabs. Following lamination, the cells were encapsulated in aluminum-plastic films and subjected to consistent external pressure using a customized fixture during electrochemical testing. The techno-economic analysis used in this study was conducted using BatPaC 5.0 modelling software.[47]

In-situ EIS measurements and DRT analysis

In-situ electrochemical impedance spectra (EIS) of Zn–I_2 coin cell were measured by VMP3 Biologic potentiostat. All cells were rested for 1 h after assembly to allow electrodes to be well infiltrated. The cells were first fully discharged to 0.6 V, followed by a complete charge/discharge cycle from 0.6 V to 1.8 V at a current density of 1 A g^{-1} for the capacity defining. After that, potentiostatic EIS measurements were performed at different SOC during charging and discharging, with a frequency range from 0.01 Hz to 100 kHz (10 points per decade) and an amplitude of 10 mV at open circuit potential. Notably, the cells need to be settled at OCV for 30 min after bringing the cell to the required SoC to reach equilibrium. To understand the impedance trend observed during charging and discharging, distribution of relaxation time (DRT) analysis was used to decouple the entangled processes governing the EIS spectra. Open-source MATLAB script-based software (DRT Tools) developed by Francesco Ciucci's group was utilized.[53]

Quantum chemistry calculations

The models were constructed and optimized using the Gaussian 16. Geometric and energy optimizations were performed at the B3LYP/6-31G(d) theoretical level, with dispersion correction and frequency calculations conducted using DFT-D3. The electrostatic potential (ESP) was created by GaussView 6.0. The first-principles calculations were carried out using the Vienna Ab initio Simulation Package (VASP). The exchange-correlation potential was treated by using a generalized gradient approximation (GGA) with the Perdew-Burke-Ernzerhof (PBE) parametrization. A cutoff energy of 450 eV was applied for the plane-wave basis set in all calculations. The convergence tolerance of geometry optimization was set as 1.0×10^{-5} eV for energy, and all the forces on each atom were smaller than 0.02 eV $Å^{-1}$. The binding energy (E) between I^+ and amide molecule is defined by the following equation:

$$E = E_{total} - (E_A + E_B)$$

Molecular dynamics simulation

The molecular dynamics simulations were performed using the LAMMPS package.[54] The OPLS-AA force field was selected in this work, which is good for the investigation of various small organic molecules. Water molecules were simulated with the SPC/E model. The partial charges on atoms were obtained using the restrained electrostatic potential (RESP) method which was calculated with Multiwfn software. The electrolyte system was initialized using the Packmol package and the Moltemplate package.[55,56] Periodic boundary conditions were applied in the x, y, and z directions, and short-range electrostatic interactions were treated using a 1.2 nm cutoff. The systems were initially annealed from 500 to 298.15 K over 0.1 ns in the NVT ensemble, followed by a 2.0 ns NPT run at 298.15 K as the pressure was lowered from 10 to 1 atm. Equilibration proceeded in the following steps: (1) NVT annealing from 500 to 298.15 K over 0.1 ns; (2) NPT equilibration at 298 K and 10 atm for 1 ns; (3) NVT relaxation at 298 K for 1 ns; (4) NPT relaxation for 2 ns at 298 K while reducing the pressure from 10 to 1 atm; (5) NPT relaxation at 298 K and 1 atm for 2 ns; and (6) NVT equilibration at 298 K for 10 ns. After relaxation, the electrode (comprising three Zn layers and three graphite layers) was oriented parallel to the XY plane and kept frozen in all atomistic simulations. A constant potential of 1.8 V was then applied to the cathode, and the system was further equilibrated for 5 ns under NVT conditions at 298 K.[57−60] Temperature coupling was achieved using the Nosé–Hoover thermostat, whereas pressure coupling was regulated via the Berendsen barostat.

Techno-economic analysis

The levelized cost of storage (LCOS) quantifies the discounted cost per unit of discharged electricity for a specific storage technology and application. This metric is calculated according to the following equation:

$$LOCS = \frac{CAPEX + OPEX + FUEL}{E_{discharge}}$$

where CAPEX refers to the initial capital investment incurred in the first year, comprising inside battery limits (ISBL), outside battery limits (OSBL), engineering and construction costs. OPEX accounts for annual operational cash costs, including labor, maintenance, property taxes, insurance, and plant overhead, along with periodic cell replacement costs triggered by capacity degradation over the system economic life. FUEL represents the electricity cost required for charging. $E_{discharge}$ represents the cumulative lifetime discharged electricity of the energy storage system, which is calculated by multiplying the rated energy capacity, annual cycles, economic life and round-trip efficiency. The techno-economic analysis is based on a 1 MW energy storage system operating in energy arbitrage scenario. Discharge duration is configured to 2 hours to address demand peaks. The operational schedule adopts a twice-daily cycling regime (off-peak charging and peak discharging) to match the typical dual morning and evening demand peaks, resulting in annual cycles of 730. The project's economic life is set to 20 years.

References

(53) Wan, T. H.; Saccoccio, M.; Chen, C.; Ciucci, F. Influence of the Discretization Methods on the Distribution of Relaxation Times Deconvolution: Implementing Radial Basis Functions with DRTtools. *Electrochim. Acta* **2015**, *184* (1), 483–499.

(54) Thompson, A. P.; Aktulga, H. M.; Berger, R.; Bolintineanu, D. S.; Brown, W. M.; Crozier, P. S.; in 't Veld, P. J.; Kohlmeyer, A.; Moore, S. G.; Nguyen, T. D.; Shan, R.; Stevens, M. J.; Tranchida, J.; Trott, C.; Plimpton, S. J.; LAMMPS - A Flexible Simulation Tool for Particle-Based Materials Modeling at the Atomic, Meso, and Continuum Scales. *Comput. Phys. Commun.* **2022**, 271, 108171.

(55) Martinez, L.; Andrade, R.; Birgin, E. G.; Martinez, J. M. Packmol: A Package for Building Initial Configurations for Molecular Dynamics Simulations. *J. Comput. Chem.* **2009**, *30* (13), 2157–2164.

(56) Jewett, A. I.; Stelter, D.; Lambert, J.; Saladi, S. M.; Roscioni, O. M.; Ricci, M.; Autin, L.; Maritan, M.; Bashusqeh, S. M.; Keyes, T.; Dame, R. T.; Shea, J.-E.; Jensen, G. J.; Goodsell, D. S. Moltemplate: A Tool for Coarse-Grained Modeling of Complex Biological Matter and Soft Condensed Matter Physics. *J. Mol. Biol.* **2021**, *433* (11), 166841.

(57) Dufils, T.; Jeanmairet, G.; Rotenberg, B.; Sprik, M.; Salanne, M. Simulating Electrochemical Systems by Combining the Finite Field Method with a Constant Potential Electrode. *Phys. Rev. Lett.* **2019**, *123*, 195501.

(58) Raiteri, P.; Kraus, P.; Gale, J. D. Molecular Dynamics Simulations of Liquid–Liquid Interfaces in an Electric Field: The Water–1,2-Dichloroethane Interface. *J. Chem. Phys.* **2020**, *153*, 164714.

(59) Scalfi, L.; Limmer, D. T.; Coretti, A.; Bonella, S.; Madden, P. A.; Salanne, M.; Rotenberg, B. Charge Fluctuations from Molecular Simulations in the Constant-Potential Ensemble. *Phys. Chem. Chem. Phys.* **2020**, *22* (19), 10480–10489.

(60) Dufils, T.; Sprik, M.; Salanne, M. Computational Amperometry of Nanoscale Capacitors in Molecular Simulations. *J. Phys. Chem. Lett.* **2021**, *12* (18), 4357–4361.

Figures

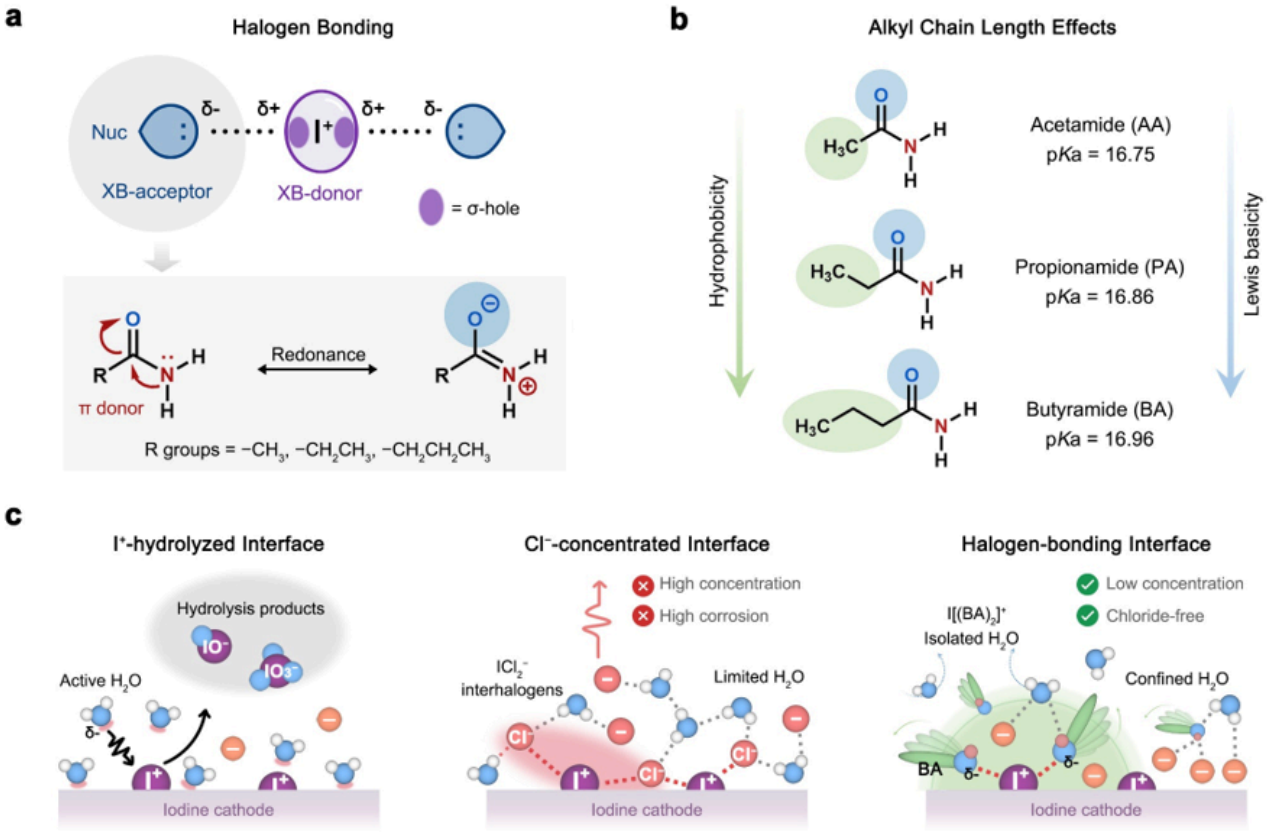

Figure 1

Schematic illustrations of (a) the halogen bond interactions between amide acceptors and I^+ species, (b) the amide alkyl chain length effects, and (c) a comparison of interfacial reaction mechanisms among traditional electrolyte, high-concentration chloride electrolyte, and the proposed halogen-bonding chloride-free electrolyte.

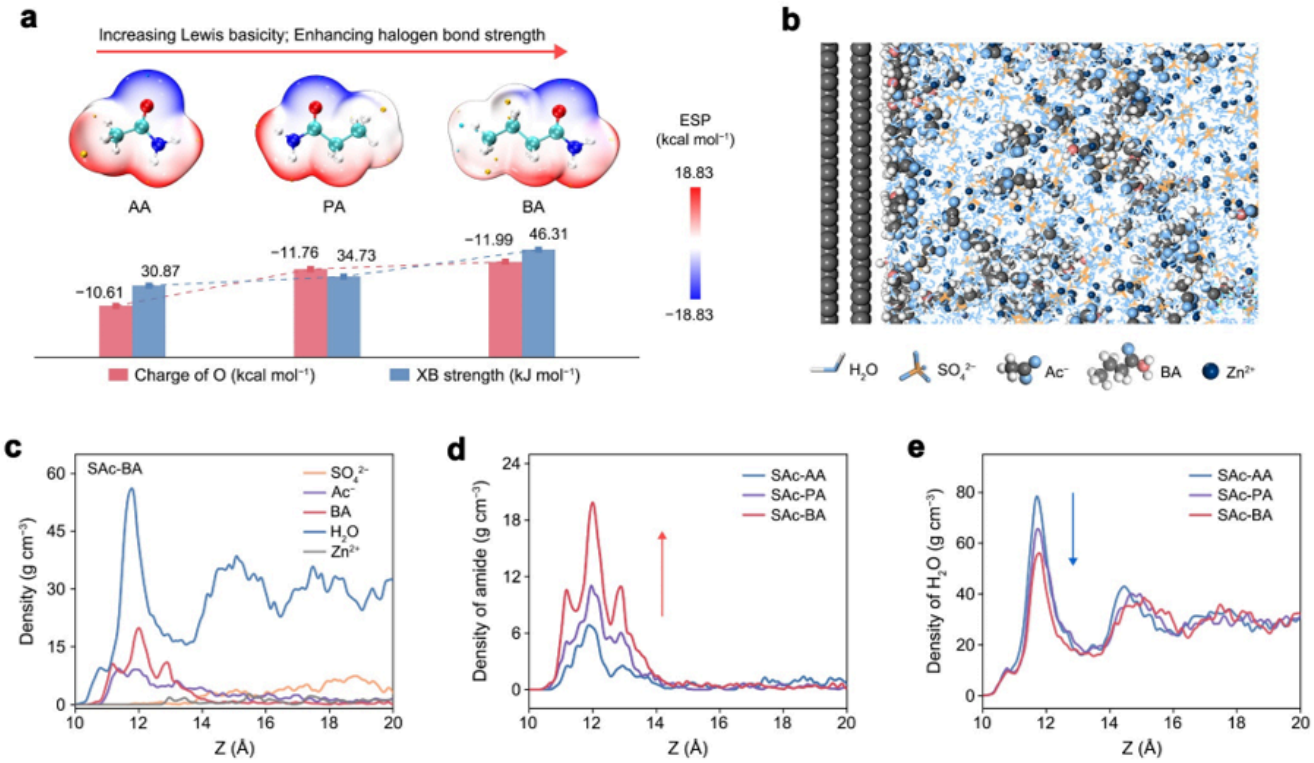

Figure 2

Multiscale simulations of molecularly tailored halogen-bonding interface. (a) Molecular electrostatic potential maps, charge of carbonyl oxygen and halogen bond strength of AA, PA and BA. (b) Snapshots of the cathodic interfacial structure and (c) radial density distribution in the SAc-BA electrolyte within 2 nm to the cathode at 1.8 V *versus* Zn^{2+}/Zn. Radial density distributions of (d) amide and (e) water molecules in different amide-modified SAc electrolytes within 2 nm to the cathode at 1.8 V *versus* Zn^{2+}/Zn.

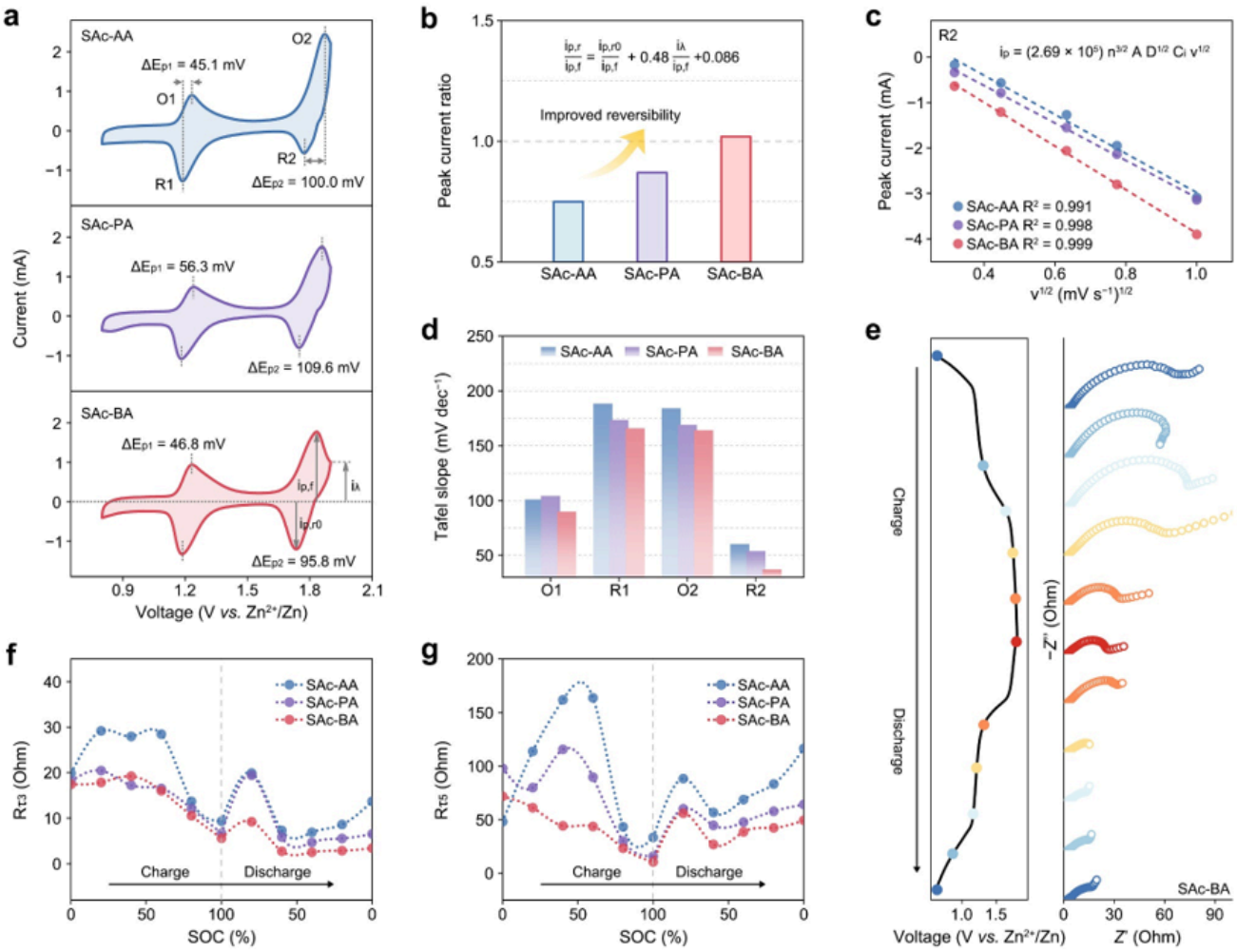

Figure 3

Electrochemical assessment of iodine conversion reversibility. (a) CV curves of Zn–I_2 cells at a scan rate of 0.2 mV s^{-1}, (b) peak current ratio of R2/O2 based on Nicholson's method, (c) the function of R2 peak current and square root of scan rate to fit the Randles–Sevcik equation, (d) Tafel slope values of iodine redox reactions, (d), (e) *in situ* EIS of Zn–I_2 cells and (f, g) resistance values at different SOC in different amide-modified SAc electrolytes.

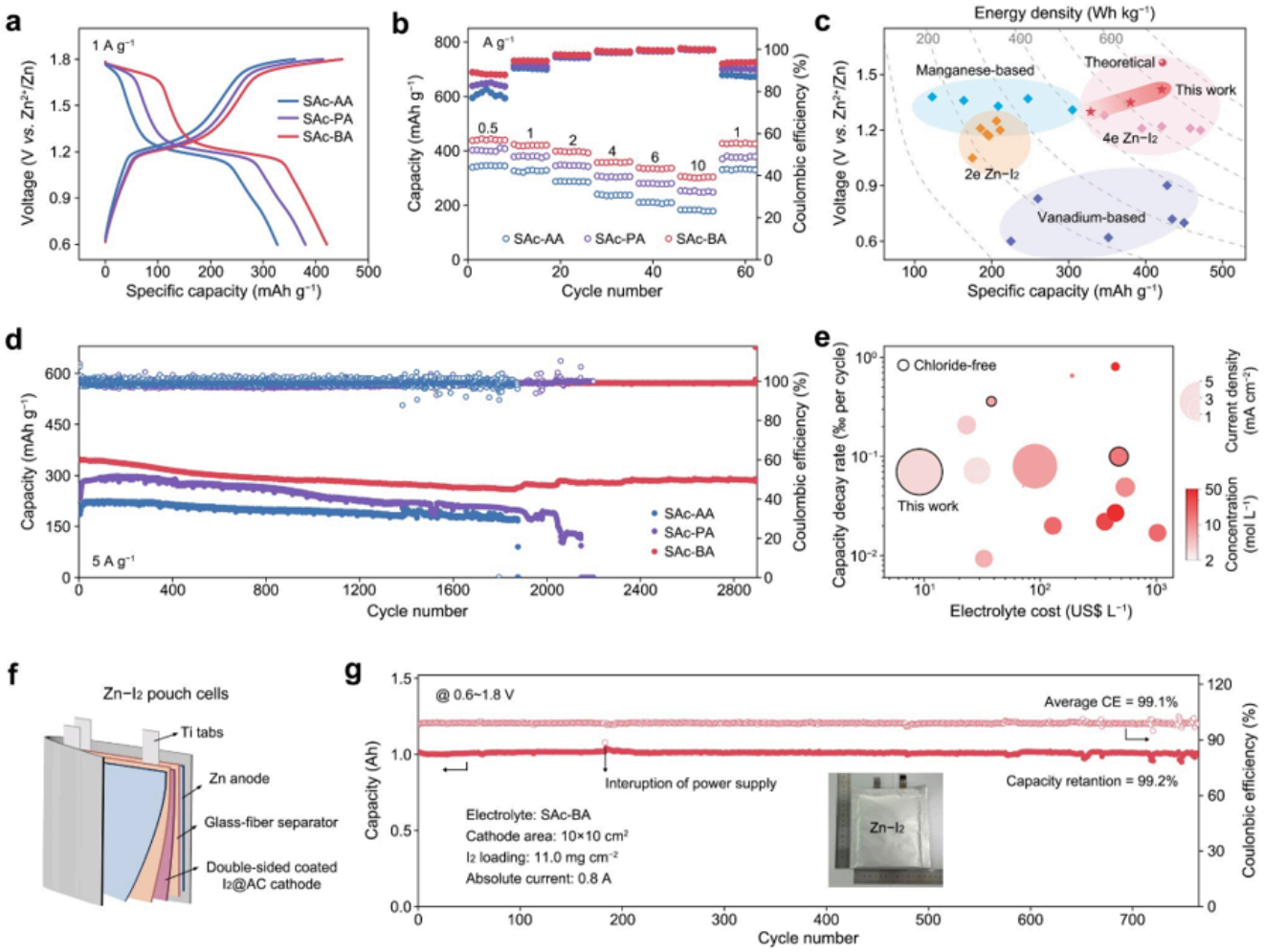

Figure 4

Electrochemical performance of four-electron Zn–I_2 batteries. (a) Galvanostatic voltage profiles at a current density of 1 A g^{-1} and (b) rate performances in different amide-modified SAc electrolytes. (c) Comparisons of the average output voltage, capacity and energy density with the reported aqueous zinc-based batteries. (d) Cycling performances in different amide-modified SAc electrolytes at a current density of 5 A g^{-1}. (e) Comparison of electrolytes cost, concentrations and electrochemical performances of reported aqueous Zn–I_2 batteries. (f) Schematic diagram and (g) cycling performances of Zn–I_2 pouch cells, inset shows corresponding digital image.

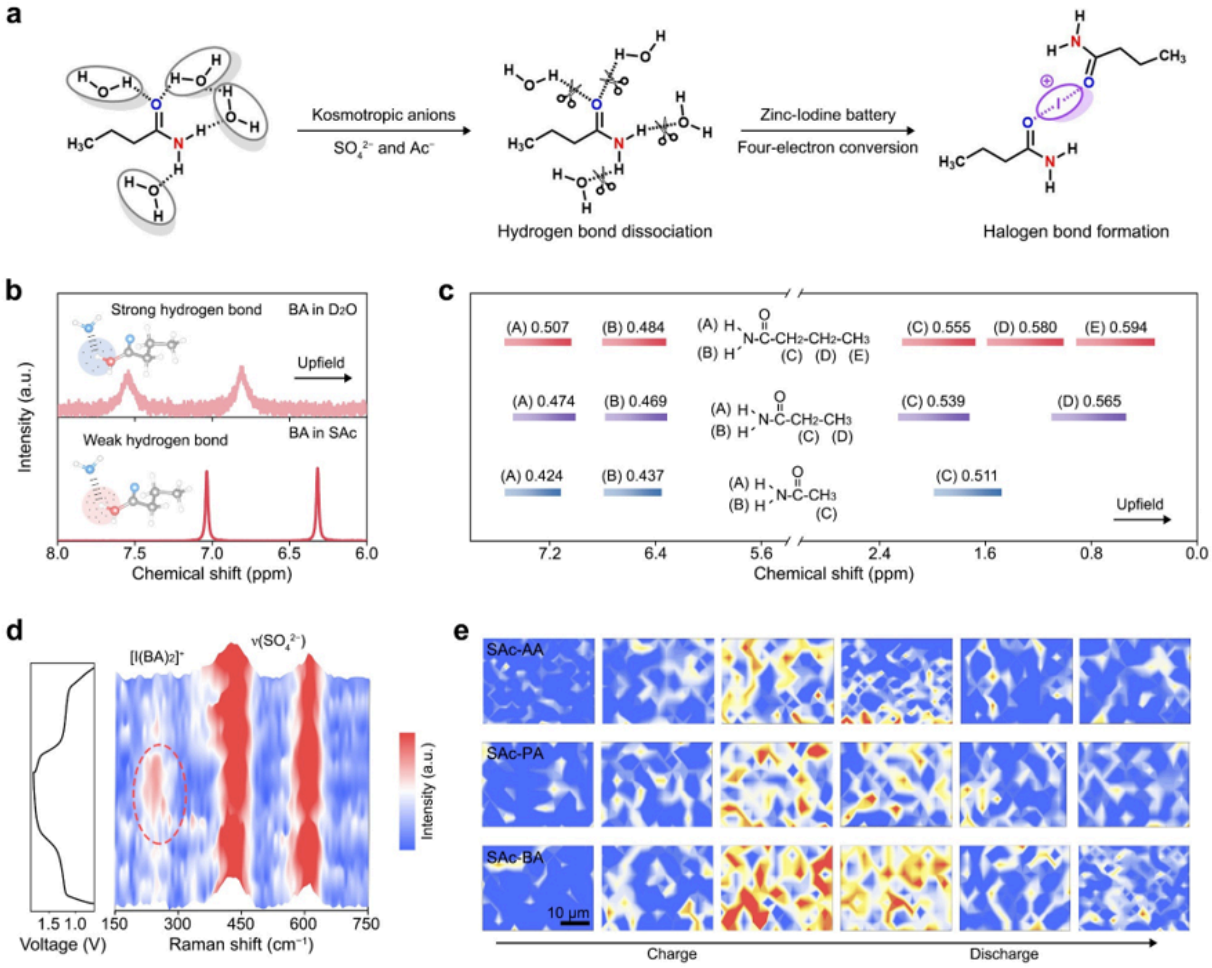

Figure 5

Spectroscopic evidence of the halogen bond stabilization mechanism. (a) Schematic representation of the hydrogen bond dissociation and the halogen bond formation. (b) ^{1}H NMR shift of the protons on the amino group of BA molecules and (c) the chemical shift values of the protons on different amide molecules after introducing kosmotropic anions. (d, e) *In situ* Raman spectra and mappings of the Zn–I_2 cells with different amide-modified SAc electrolytes.

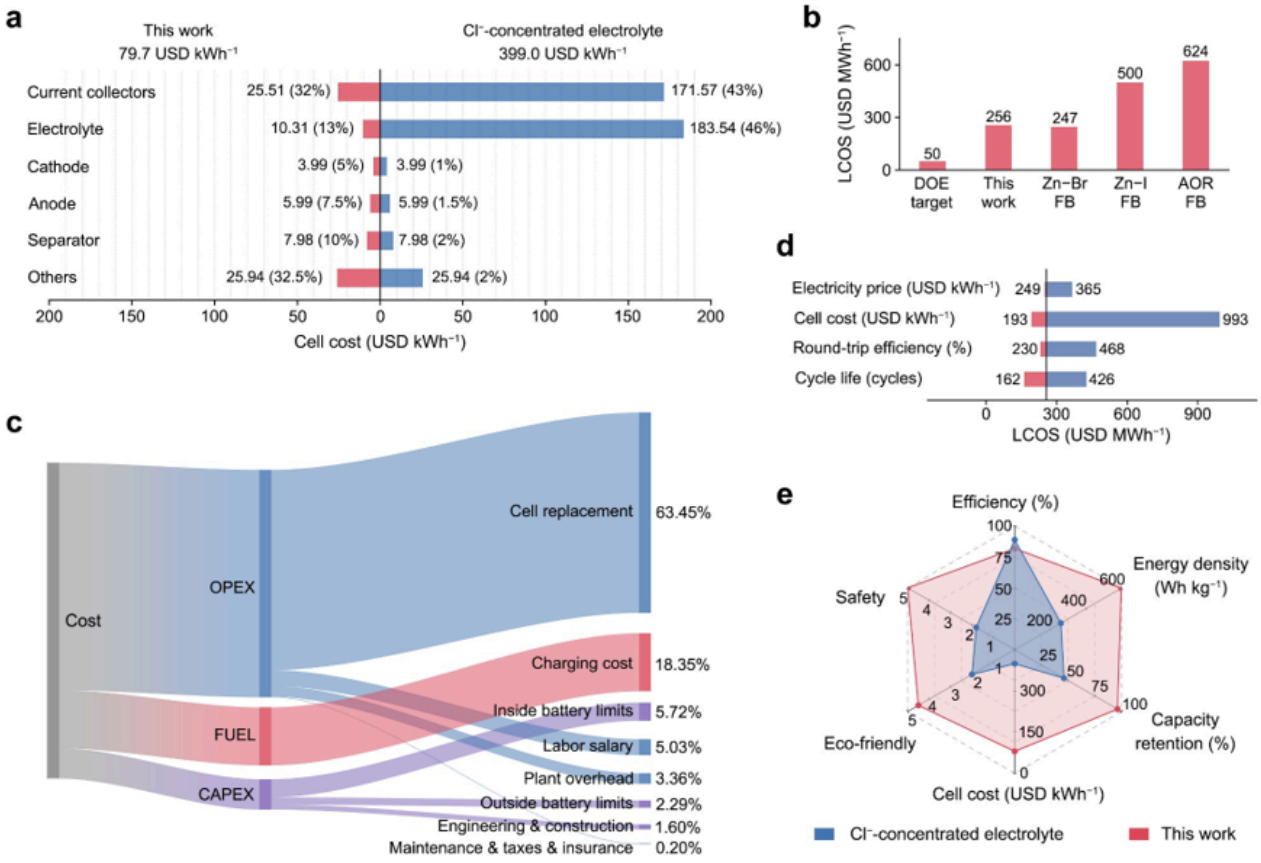

Figure 6

Techno-economic assessment of four-electron Zn–I_2 batteries. (a) Cell cost comparison between Cl^--concentrated electrolyte and halogen-bonding chloride-free electrolyte. (b) LCOS comparison among aqueous battery technologies, benchmarked against the DOE target. (c) Cost breakdown and (d) sensitivity analysis of LCOS for halogen-bonding chloride-free system. (e) Comparison of key performance indicators for different electrolyte configurations.

Supplementary Files

This is a list of supplementary files associated with this preprint. Click to download.

- SI.docx